Accepted Manuscript

Effects of Zr on the amorphization of Cu-Ni-Zr alloys prepared by mechanical alloying

C. Martínez, C. Aguilar, F. Briones, D. Guzmán, E. Zelaya, L. Troncoso, P.A. Rojas

Please cite this article as: C. Martínez, C. Aguilar, F. Briones, D. Guzmán, E. Zelaya, L. Troncoso, P.A. Rojas, Effects of Zr on the amorphization of Cu-Ni-Zr alloys prepared by mechanical alloying, *Journal of Alloys and Compounds* (2018), doi: 10.1016/j.jallcom.2018.04.259.

This is a PDF file of an unedited manuscript that has been accepted for publication. As a service to our customers we are providing this early version of the manuscript. The manuscript will undergo copyediting, typesetting, and review of the resulting proof before it is published in its final form. Please note that during the production process errors may be discovered which could affect the content, and all legal disclaimers that apply to the journal pertain.

Effects of Zr on the amorphization of Cu-Ni-Zr alloys prepared by mechanical alloying

C. Martínez[a*], C. Aguilar[b], F. Briones[c], D. Guzmán[d], E. Zelaya[e], L. Troncoso[f], P. A. Rojas[g]

[a] Laboratorio de Corrosión, Instituto de Química, Pontificia Universidad Católica de Valparaíso, Av. Universidad 330, 3100000, Valparaíso, Chile

[b] Departamento de Ingeniería Metalurgia y Materiales, Universidad Técnica Federico Santa María, Av. España 1680, 2390123, Valparaíso, Chile

[c] Escuela de Ingeniería Mecánica, Pontificia Universidad Católica de Valparaíso, Los Carrera 01567, 2430120, Quilpué, Chile

[d] Departamento de Metalurgia, Universidad de Atacama, Av. Copayapú 485, 1531772, Copiapó, Chile

[e] Centro Atómico Bariloche-CNEA, Av. E. Bustillo 9500, 8400, San Carlos de Bariloche, Argentina

[f] Instituto de Materiales y Procesos Termomecánicos, Universidad Austral, General Lagos 2086, 5111187, Valdivia, Chile

[g] Escuela de Diseño, Universidad Adolfo Ibáñez, Diagonal Las Torres 2640, 7941169, Santiago, Chile

*Corresponding authors: carola.martinezu@usach.cl

Laboratorio de Corrosión, Instituto de Química, Pontificia Universidad Católica de Valparaíso, Av. Universidad 330, Valparaíso, Chile

Phone: +56-9-87325288

Abstract

This work presents the effects of high energy milling with different Ni and Zr ratios on the amorphization of ternary Cu-Ni-Zr alloys (initially, Cu-43Ni-7Zr, Cu-12Ni-31Zr, Cu-33Ni-7Zr, and Cu-12Ni-23Zr; and later, Cu-23Ni-15Zr and Cu-11Ni-7Zr). Microstructure was determined using X-Ray diffraction and electron microscopy. Results were compared to thermodynamic models. In the ternary alloys under study, the lattice parameter of the Cu-Ni solid solution was generally correlated to the amounts of nickel incorporated into the Cu lattice. However, longer milling times reduced that lattice parameter and facilitated Zr insertion into the solid solution. For example, after 5 h of milling time, microstructural analysis showed the formation of a solid solution with cubic structure in Cu-43Ni-7Zr. This pattern is consistent with the presence of a lattice parameter between that of Cu and Ni (α–phase); in contrast, the Cu-33Ni-7Zr alloy showed an α-phase and another similar to Zr. Results suggest that, as the amount of nickel increases, the ability to form an amorphous phase decreases. Additionally, experimental and thermodynamic data showed a solid-solution formation stage, followed by an amorphous phase formation stage that occurred as milling time and Zr content increased.

1. Introduction

Since the discovery of metallic glasses in the 1960s [1], extensive experimental and theoretical efforts have been made to study the glass-forming ability of metallic alloy

systems. Interest has especially culminated in recent decades, and particularly on amorphous solid solutions, known as bulk metallic glasses (BMG) for their high glass-forming ability and fabricated by rapidly quenching, melted metallic compounds to ensure random atomic arrangement in a non-equilibrium state [2]. That said, there are also methods of amorphizing solids without their passing through liquid states, such as irradiation, hydrogen-assisted amorphization, interdiffusion of elemental metals, and mechanical alloying (MA) [3]. These are known as solid-state amorphization reactions (SSARs). Amorphous alloys have huge potential as advanced engineered materials due to diverse characteristics, such as high elasticity, hardness, and resistance to corrosion and wear [4]. Considering this potential, numerous studies have been performed in order to attempt to optimize fabrication processes (both traditional and new), thus improving these already unique properties. As such, the study of amorphous materials and alternative fabrication methods has become one of the most important fields in contemporary material science.

Of these amorphous materials, Cu-based alloys, and their mechanical properties in particular, have been garnering interest in recent years [5], some Cu-based BMGs have been shown to have compressive strength of up to 2 GPa [6], while others may form BMG alloys with impressive ductility [7,8]. Cu-based amorphous materials are mainly made through conventional casting techniques, where the cooling rate of molten metal must be faster than the critical cooling rate for forming amorphous alloys. As such, the amounts of amorphous material produced as BMGs are limited. In looking at alternative methods, it has been demonstrated that milling processes produce a variety of microstructural changes. Indeed, this process has produced a variety of non-equilibrium phases, such as super-saturated solid solutions, intermediate metastable phases, quasi-crystalline alloys,

nanostructured materials, and metallic glasses [9–11]. In other amorphous alloys of note, Cu-Zr based BMGs have attracted attention due to their high strength and high thermal stability against crystallization, with lower costs than Zr-based BMGs [12]. Previous studies [13–15] have shown crystallinity differences in Cu-Ni and Cu-Zr phases under the same high-energy milling processes. However, since many microstructural changes overlap during mechanical alloying, the exact nature of these changes remains unclear. In this regard, very few works have focused on two relevant aspects: i) obtaining microstructural information via X-ray diffraction analysis, such as crystallite size, microstrain, dislocation factor contrast, etc.; and ii) describing the thermodynamic relationship between solid solution formation and solid state amorphization.

Therefore, the work discusses microstructural changes in mechanically alloying within systems of all three of the elements discussed above. The thermodynamic and X-ray profile analyses of the microstructural changes provided in this paper may thus lead to a better understanding of the formation stages in Cu-based amorphous alloys during mechanical alloying.

2. Material and methods

Mechanical alloying was performed with pure powders: Cu (99.7% at., < 63 mesh, Merck), Ni (99 % at., < 230 mesh, Merck), and Zr (99.8% at., < 50 mesh, Noah Technologies). Milling was carried out with different powder ratios: initially, Cu-43Ni-7Zr, Cu-12Ni-31Zr, Cu-33Ni-7Zr, and Cu-12Ni-23Zr; and later, Cu-23Ni-15Zr and Cu-11Ni-7Zr (at. %). The compositions were chosen according to thermodynamic analysis, which will be discussed later. High-energy milling was performed in a SPEX 8000D with stainless steel containers and balls (balls diameters: 12 and 9 mm). The BPR in all cases was 10:1. The containers

were filled in a glove box under argon atmosphere, and included 1 % wt. stearic acid as control agent. Each alloy was milled variably from 1 to 60 hours. After milling, powders were removed from the containers in an Ar-filled glove box.

The milled samples were then characterized by X-ray diffraction (XRD) to identify phase and assess phase purity. Characterization was performed with a Shimadzu XRD 6000 diffractometer (40 kV, 30 mA) in Bragg-Brentano reflection geometry with Cu-Kα_1 ($\lambda =$ 1.5406 Å) and Cu-Kα_2 ($\lambda =$ 1.5444 Å) radiation. The counting time for each pattern was 3 h. Diffraction data were analyzed using the Rietveld method [16] with the FULLPROF program [17]. The line shape of the diffraction peaks was generated by a pseudo-Voigt function. The following parameters were refined: background points, zero shift, half width, pseudo-Voigt, thermal factor, scale factor, and unit-cell. Crystallite size and microstrain was determined via traditional/modified Williamson-Hall and traditional/modified Warren-Averbach methods and model [18–20]. Iron content was measured using a GBS 905 atomic absorption spectrometer. Microstructure was analyzed by scanning electron microscopy (SEM) on a Zeiss EVO MA 10. Particle size was determined through image analysis using Image J software. In addition, transmission electron microscopy (TEM) was carried out in a FEI CM-200T TEM and a FEI Tecnai F20 field emission S/TEM, both operated at 200 keV.

3. Results and Discussion

3.1 Scanning electron microscopy

The microstructures of the starting powders, and alloyed powders after 5h of milling, were observed with scanning electron microscopy (Figure 1). The shape and size of powders is initially different. Copper powders have a dendritic morphology (dendrite size of 8 µm to

113 µm). Figure 1b shows Ni powder morphology as spherulitic. In contrast, Zr powders are large agglomerates of small particles, the size of which average 300 µm. Mechanically milled powders underwent substantial changes, both in morphology and particle size. The milling process involves essential changes like deformation, cold-welding, and fractures [10]. Despite Cu, Ni, and Zr morphology and size differences, mechanical alloying promotes the formation of flakes welded over each other in all alloys. This microstructure is indeed indicative of multiple fractures and cold welding. Ternary alloys with more nickel had larger particle sizes, such as alloy Cu-43Ni-7Zr (averaging 73 µm). There was no significant correlation between particle size and composition (Table 1).
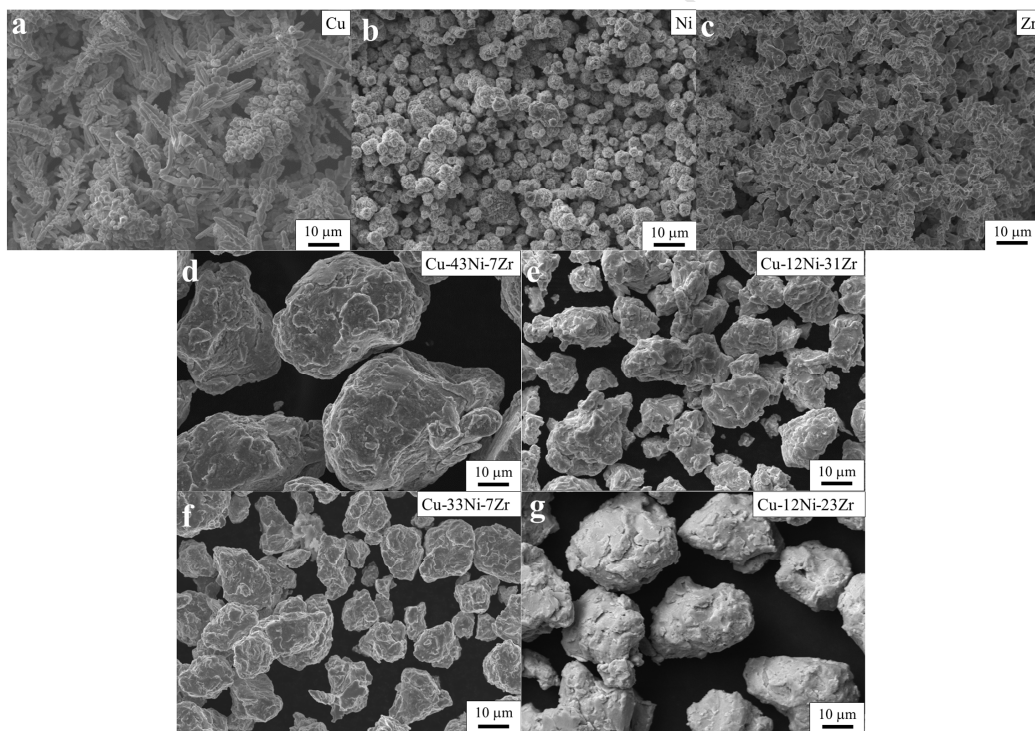

Figure 1. SEM Images of: pure elements a) Cu, b) Ni, and c), Zr; and ternary alloys at 5 h milling time d) Cu-43Ni-7Zr, e) Cu-12Ni-31Zr, f) Cu-33Ni-7Zr and g), Cu-12Ni-23Zr

Table 1. Particle sizes and morphology for pure and ternary alloy powders.

Sample	Cu	Ni	Zr	Cu-43Ni-7Zr	Cu-12Ni-31Zr	Cu-33Ni-7Zr	Cu-12Ni-23Zr
Morphology	Dendritic	Spherical	Agglomerate	Flakes	Flakes	Flakes	Flakes
Size, µm	40	4	240	73	32	33	46
Stand. Dev.	24	2	10	33	23	18	23

3.2 X-Ray diffraction analysis

The study of microstructural refinements in Cu-Ni-Zr ternary alloys following mechanical alloying was realized in order to identify the optimal conditions for system amorphization, as well as optimal amount of Zr. This is especially relevant given that Cu-Zr and Ni-Zr systems present many similarities, not only in their intermetallic phases and invariant reactions [21,22], but also their limited solid solubility.

Diffraction patterns for the ternary alloys are shown in Figure 2, where different behaviors under the same milling conditions can be observed. For alloys with greater amounts of Ni (Figures 2a and 2c), the Cu and Ni diffraction peaks begin to overlap after 1 h of milling. At 5 h of milling, there is a diffraction peak at the 2θ position, where reflections for both elements had been. The presence of this diffraction peak is evidence of the formation of a Cu-Ni solid solution, which has unlimited mutual solid solubility. The diffraction peak associated with the Cu-Ni solid solution is similar to the diffraction peak of pure Cu, which is possibly due to Ni being introduced into the Cu lattice. As milling time increases, the diffraction peaks of the solution widen and lose intensity. This is associated with microstructural refinements and the incorporation of crystalline defects due to the mechanical alloying process [23]. Additionally, diffraction peaks associated with Zr disappear over time. This may be attributable to Zr being incorporated into the Cu-Ni solid

solution lattice. Super-saturated solid solutions produced by mechanical alloying have been

widely studied [24–31]. This phenomenon can be elucidated by calculating the solid

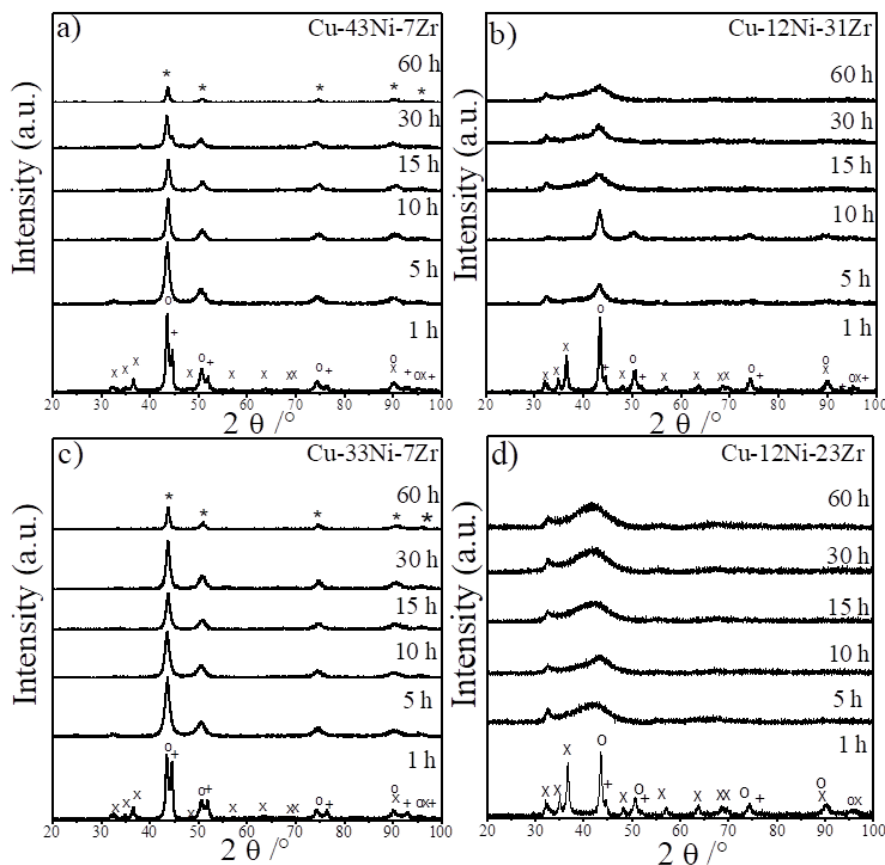solution lattice parameter, realized after Rietveld refinement.

Figure 2. XRD spectra of a) Cu-43Ni-7Zr, b) Cu-12Ni-31Zr, c) Cu-33Ni-7Zr, and

d) Cu-12Ni-23Zr alloys at different milling times. (o Cu; + Ni; x Zr *; Cu-Ni$_{SS}$)

In alloys with greater amounts of Zr (Cu-12Ni-31Zr and Cu-12Ni-23Zr), crystalline phases

were not formed. It was, however, observed that longer milling times after the first hour

resulted in a notable decrease of peak intensities in Cu, Ni, and Zr elemental powders

(Figures 2b and 2d). This loss of intensity, common for elements in this process, is

associated with a large number of defects and microstructural refinements [32–34]. After 5

hours, no diffraction peaks of the original elements were detected; only two diffracted peaks were observed: a less intense peak close to 32°, which corresponds to the widening of the Zr plane (110) as a result of the amorphization process (which has also been observed in other systems [33,35]); and another, wider peak located between 35 and 47° associated with the amorphous phase. This result, when considered with those obtained previously in a study of Cu-Zr binary alloy systems [15], suggests that, under the milling conditions employed, the system is amorphized; however, it is not totally amorphous. Rather, the system is composed of disordered zones of small crystallites. Significantly, in mixing Cu, Ni, and Zr, it is clear that the zirconium content is relevant in amorphization time.

Rietveld analysis was possible after 5 hours of milling time, using an Fm-3m model of Cu-43Ni-7Zr and Cu-33Ni-7Zr alloys (the other alloys with more Zr (Cu-12Ni-31Zr and Cu-12Ni-23Zr) could not undergo Rietveld analysis due to the loss of crystallinity after 5 hours of milling). The peak around 32° remains after 60 hours of milling, implying some quantity of zirconium in crystalline form. The amount of Zr phase in the system was 2.51(2) % of weight. In these alloys, Cu, Ni, and Zr atoms are randomly distributed around site 4a(0 0 0). Figure 3 shows the main lattice parameters of the Cu-43Ni-7Zr and Cu-33Ni-7Zr alloys. For Cu-43Ni-7Zr, the value of a_0 after 5 h of milling was 3.597(1) Å, which continued to diminish as milling time increased, towards a value of 3.592(1) Å after 30 hours of milling. This behavior can be attributed to the atomic radius of Ni, which is less than that of copper (Ni: 1.24 Å; Cu: 1.28 Å). With longer milling times, greater amounts of Ni are introduced into the copper lattice, lowering the lattice parameter of the solid solution. According to XRD observations, increased milling time (> 30 h) may cause Zr (atomic radius 1.60 Å) to be introduced into the lattice, since this is when the lattice parameter begins to increase, up

to 3.598(1) Å, at 60h. Additional contributions of increasing the lattice parameter may come from the incorporation of free volume [36,37].

Cu-33Ni-7Zr alloy presents the same behavior, i.e., increased milling time increases the lattice parameter, though in this case up to 3.610 Å after 60h of milling. The difference in the lattice parameter may be due to the fact that the Cu-33Ni-7Zr alloy contains less Ni and, therefore, can incorporate a greater amount of Zr into the lattice.
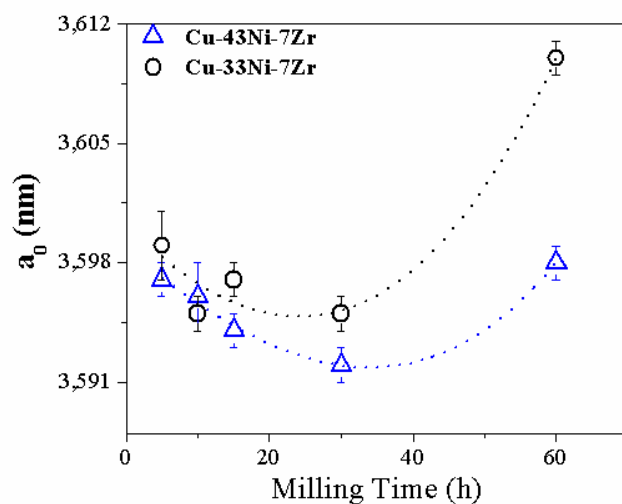

Figure 3. Lattice parameter (a_0) determined by Rietveld refinement

To better determine the influence of Zr on amorphization in a Cu-Ni-Zr system, additional alloys, Cu-23Ni-15Zr and Cu-11Ni-7Zr, were also synthesized. These were subjected to 5 hours of milling time (the minimum necessary to form a solid solution or amorphous phase). Figure 4 shows the diffraction patterns of these alloys, clearly demonstrating that the element that most influences Cu-Ni amorphization is Zr. The influence of Zr has also been reflected in other studies, e.g., recent developments of a series of multicomponent

alloys with excellent amorphization ability and high stability of formed amorphous phase
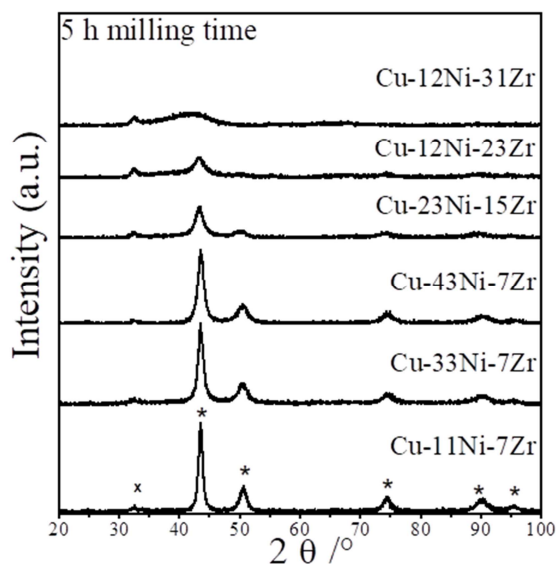against crystallization [38].

Figure 4. XRD spectra of Cu-Ni-Zr alloys at 5 h milling time under the same milling

conditions. (o Cu; + Ni; x Zr *; Cu-Ni$_{SS}$).

Of the alloys in this study, the lattice parameter of the Cu-11Ni-7Zr alloy is that which is

closest to pure copper (see Figure 5). This is due to the high percentage of copper present

in the alloy – reducing the amount of copper reduces the lattice parameter, which is

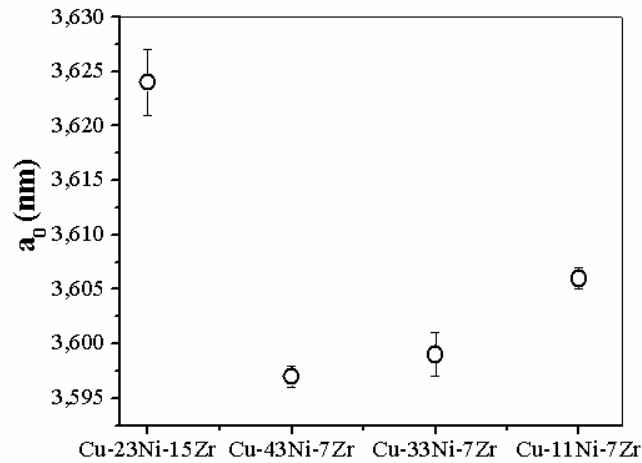associated with the formation of the solid solution as mentioned before.

Figure 5. Lattice parameter (a_0) of Cu-Ni-Zr alloys at 5 hour milling time determined by

Rietveld refinement.

The structural evolution of the Cu-based ternary alloys under study was determined through

the application of traditional/modified Williamson-Hall and traditional/modified Warren-

Averbach methods.

3.2.1. Traditional Williamson-Hall method

This method considers that peak broadening is produced by variation resulting from both

crystallite size and isotropic microstrain [39]. To separate these, we apply eq. (1), where

ς/D and ΔK^d are crystallite size and microstrain, respectively, $\Delta K = 2\cos\theta(\Delta\theta)/\lambda$, $\Delta K^d = \eta\, K$

($K = 2\sin\theta/\lambda$), θ is the Bragg angle, $\Delta\theta$ is the full width at half maximum of each peak, λ is

the wavelength of x-rays, ς is a geometrical constant that varies between 0.89 to 1.39 (for

metals and alloys, a value of 1 is used), D is the average volume crystallite size, and η is

the isotropic microstrain.

$$\Delta K = \frac{\varsigma}{D} + \Delta K^d \tag{1}$$

3.2.2. Traditional Warren-Averbach

Information on grain size and strain can be extracted from diffraction peaks represented in a Fourier series of two coefficients, A(L) and B(L), where L is the normal distance to reflecting planes. If peaks are perfectly symmetric, then B(L) is 0. A(L) can be expressed as $A(L)=A^s(L) \times A^m(L)$ were $A^s(L)$ is the contribution of crystallite size and $A^d(L)$ the contribution of isotropic microstrain. Taking the logarithm and introducing the terms for a cubic crystalline system, the traditional Warren-Averbach equation is obtained, eq. (2) [20], where $\langle \varepsilon_L^2 \rangle$ is the mean square isotropic microstrain, $h_0^2 = h^2 + k^2 + l^2$ (h, k and l are the Miller indices), and a is the lattice parameter.

$$\ln A(L) = \ln A^s(L) - 2\pi \langle \varepsilon_L^2 \rangle L^2 \frac{h_0^2}{a^2} \tag{2}$$

3.2.3. Modified Williamson-Hall method

Modified Warren–Averbach and Williamson–Hall methods were applied to analyze the X-ray diffraction peaks [19]. These methods are used in the presence of anisotropic microstrain in materials, and incorporate one dislocation model of strain anisotropy based on the contrast of dislocations (C), which vary with the relative orientation of the Burgers vector (**b**), line vectors of dislocations (l), and the diffraction vector (**g**), similarly to transmission electron microscopy [23]. Eq. (3) gives the modified Williamson-Hall equation [19], where A is a parameter determined by the effective outer cut-off radius of dislocations (Re), ρ is the dislocation density, $K=2\sin\theta/\lambda$, and $<C>$ is the average dislocation contrast factor for a particular reflection. Eq. (3) shows that if the dislocations

are the primary source of strain in a crystal, the proper scaling factor of the breadth of line profile is $K<C>^{1/2}$ instead of K (K is equal to the diffraction vector at the exact Bragg position).

$$\Delta K = \frac{\varsigma}{D} + \left(\frac{\pi A^2 b^2}{2} \right)^{\frac{1}{2}} \rho^{\frac{1}{2}} \left(K \langle C \rangle^{\frac{1}{2}} \right) + O\left(K^2 \langle C \rangle \right) \tag{3}$$

3.2.4. Modified Warren-Averbach method

Eq. (4) is the modified Warren-Averbach method [19], where $L=na_3$ is a distance normal to the reflecting planes $\{hkl\}$, n is the harmonic number, $a_3 = \lambda/2(\sin\theta_2 - \sin\theta_1)$, $(\theta_2 - \theta_1)$, the angular range of the measured diffraction profile, $B = \pi b^2/2$, and O is the correlation factor that stands for higher order terms in $K^4 <C>^2$.

$$\ln A(L) = \ln A^s(L) - \rho B L^2 \ln\left(\frac{Re}{L} \right) \left(K^2 \langle C \rangle \right) + O\left(K^4 \langle C \rangle^2 \right) \tag{4}$$

The real part of the Fourier coefficients, A(L) are plotted against $K^2<C>$ and are fit to a parabolic equation for each L value. The intersections of the quadratic curves at K=0 provide crystallite size (the values of $A^S(L)$ are plotted against L, from which crystallite size can be determined from the interception of the initial slope on the L-axis). The modified Warren-Averbach method provides an area-weighted average crystallite size. The dislocation density, ρ, can be determined from slopes of the quadratic curves [19]. Figure 6 shows a comparison of results obtained by both traditional/modified Williamson-Hall methods for the Cu-33Ni-7Zr alloy milled at 5 h. The ΔK values of the {111} and {222} peaks are less than other peaks when the traditional Williamson-Hall method was applied (Figure 6a). This is due to the presence of anisotropic strain in the alloys; therefore, ΔK is not a linear function of K and thus, the traditional Williamson-Hall method does not

approximate ΔK well. This behavior was observed in all Cu-based alloys. On other hand, when the modified Williamson-Hall method was used (Figure 6b), two effects were observed: i) ΔK values shift upwards and the slope increases as a function of milling time, indicating a decrease of crystallite size and an increase in microstrain; and ii), ΔK values follow smooth curves as a function of $K<C>^{1/2}$, and thus ΔK does not increase monotonically with the order of reflections. Similar behavior was found for all alloys. This shows that Cu-based alloys contain anisotropic strain caused by dislocations. The traditional method assumes that strain in the materials is at random (where root-mean square is used); modified methods, that the relative atom displacement due to strain, is not. Thus, given the long range correlations between displacements, the contrast factor in the latter better represents the strain in the materials under study [19]. During MA, highly plastic deformation of Cu-based alloys occurs due to the impact of balls increasing the density of crystalline defects, like dislocations, crystallite size boundaries, stacking faults, twins, and vacancies [40]. Based then on this anisotropic strain produced by dislocations during milling, the modified Warren-Averbach and Williamson-Hall methods better interpret the information than do traditional methods.
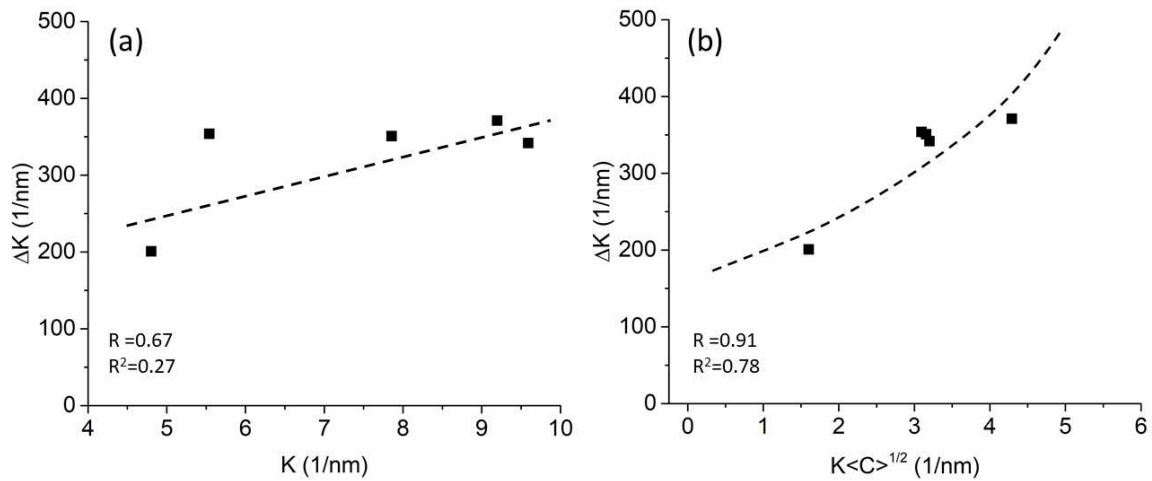
Figure 6. (a) Plot of traditional Williamson-Hall method and (b) plot of modified Williamson-Hall method, for Cu-33Ni-7Zr milled at 5 hours.

Figure 7 gives the evolution of crystallite sizes and root-mean-squared microstrains for Cu-33Ni-7Zr and Cu-43Ni-7Zr alloys determined by modified Williamson-Hall and Warren-Averbach methods. Cu-12Ni-31Zr and Cu-12Ni-23Zr alloys were not analyzed using this method, since they did not have crystalline phases. Crystallite size decreases and microstrain increases as a function of milling time in both alloys. The trend of crystallite size for both alloys observed is: i) between 0 to 15 h of milling, size decreases from 80, to around 10 and 20, nm; and ii), after sufficiently long milling times, crystallite size remains constant. On other hand, microstrains increase until 10 h of milling, to around 2.2 ($<\varepsilon^2>^{1/2}$), and afterwards remain constant. The $<\varepsilon^2>^{1/2}$ values are slightly higher for the Cu-43Ni-7Zr alloy than for the Cu-33Ni-7Zr alloy. Furthermore, the difference in crystallite size between both alloys is negligible, which suggests that Zr content does not influence crystallite size.

Next, microstrain is produced by the presence of dislocations due to solute atoms having entered the solution and moving the atoms closest to the crystal lattice into equilibrium positions. Indeed, microstrain causes an increase in local energy and, therefore, of the internal energy of the system; this, in turn, attracts solute atoms into the solid solution to decrease the local energy, and produces a fault. The presence of Zr greatly promotes crystalline defects in the structure, inducing more defects in the systems in which it is present – these crystalline defects are what promote amorphization system, and it is expected that greater amounts of Zr creates greater structural disorder.
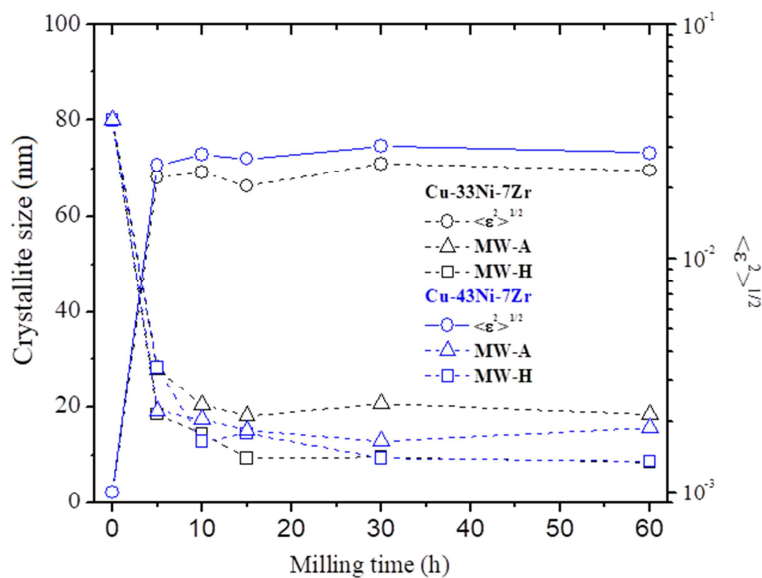

Figure 7. Evolution of crystallite size and root-mean-squared microstrains of (a) Cu-33Ni-7Zr and (b) Cu-43Ni-7Zr determined through of modified Williamson-Hall (MW-H) and modified Warren-Averbach (MW-A).

3.3 Transmission electron microscopy

Figure 8 shows bright field, dark field, and selected area diffraction (SAD) images of Cu-43Ni-7Zr and Cu-12Ni-31Zr alloys at 5 h milling time. The bright field and dark field micrographs (Figures 8a and 8b) reveal compact microstructure with very uneven crystallite sizes (between 0.6 and 25.6 nm, with an average crystallite size of 7.1 ($\pm$ 3.7) nm over a total of 350 measured crystallites). The measurements here are smaller than those made with X-Ray (Figure 7). However, this disparity could be attributed to two different effects. First, the detectability limit of X-Ray is above 5 nm. Therefore, crystallite sizes smaller than 5 nm could not be taken into account in X-Ray measurements. The histogram of crystallite size distribution measured by TEM indicates that 103 of 350 crystallites measured were smaller than 5 nm. Second, particles measured by TEM cannot be thicker than 400 nm. If larger crystallites were to have been distributed preferentially in areas of particles thicker than this value, they could not be taken into account in TEM measurements. The Energy Dispersive Spectroscopy (EDS) of the particles is also consistent with the presence of Cu, Ni, and Zr. Quantifying particles gives average values of 57% Cu, 37% Ni, and 6% Zr (% at.). This value is very close to the nominal value, and expected given TEM errors; overestimation of Cu, for example, may be due to the presence of Cu in the grid holding the sample or the inner parts of the TEM. Next, Figure 8c shows a typical selected area diffraction (SAD) of Cu-43Ni-7Zr particles. The indexation of the ring pattern is consistent with the presence of an α−phase (Fm3m). The lattice parameter measured using SAD yields a value between those of Cu and Ni, and within the experimental errors of the value measured via X-Ray diffraction. Some isolated diffractions are observed as well, which are attributable to the presence of Cu_2O in lesser amounts, an

impurity not detected by X-ray diffraction (indicated by solid white arrows). The dashed

white arrow in the figure points out a partial thickening of one of the rings, attributable to

the texture of, or strong internal tensions in, the material.

Of the Cu-12Ni-31Zr particles observable by TEM, the bright field and dark field images

show well-defined crystallites, as can be seen in Figures 8d-e. Although some well-faceted

crystallites of 200 nm diameter are present, there are also crystallites orders of magnitude

smaller, ranging from 5 to 270 nm. It should be also mentioned that 30 % of particles

showed no contrast at all, whose EDS indicated larger amounts of Zr than average. The

average crystallite size is of 47 ($\pm$ 39) nm, taken from a total of 300 crystallites measured.

All rings in the SAD (Figure 8f) can be consistently indexed with the presence of Cu and

Zr. Ni was not indexed, since its lattice parameter is close to that of Cu. Although Zr was

not detected in some particles, the great majority of them had an average compositional

value of 71% Cu, 12% Ni, and 17% Zr (% at.). The discrepancy between the nominal value

and the one measured by EDS could be attributed to those particles that were outside of the

measureable range having higher amounts of Zr. These particles could be associated with

an amorphization process that selects for particles with higher amount of Zr, and could also

explain the lack of well-defined peaks in the X-Ray diffractogram in Figure 2b. Moreover,

some particles that contribute to the SAD pattern in Figure 8f are outside XRD detectability
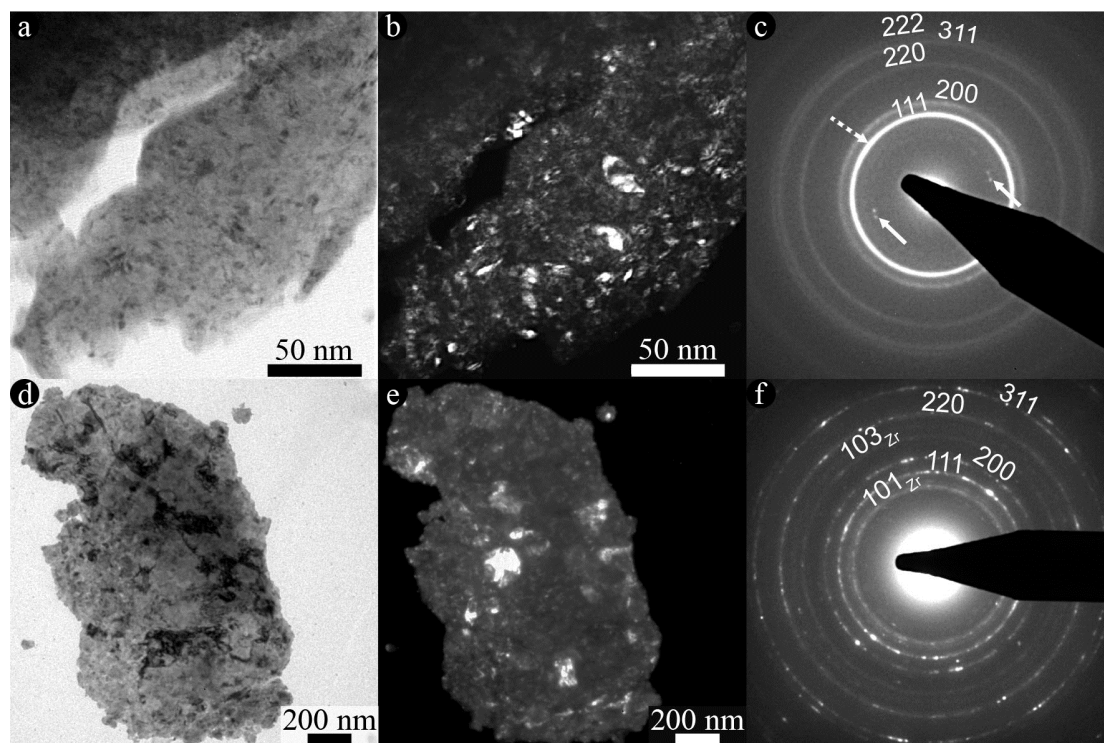
range.

Figure 8. Images of bright field, dark field, and SAD of ternary alloy particles at 5 h milling time. For Cu-43Ni-7Zr: a) bright field, b) dark field, c) SAD. For Cu-12Ni-31Zr: d) bright field e) dark field, and f) SAD.

Figure 9 shows images of bright field, dark field, high resolution transmission electron microscopy (HRTEM) and selected area diffraction (SAD) of alloys Cu-33Ni-7Zr and Cu-12Ni-23Zr at 5 h milling time. The Cu-33Ni-7Zr alloy is essentially composed of two types of particles. The most abundant have SAD similar to that of Cu-43Ni-7Zr (Figure 8f); however, the presence of two sets of rings and two tenuous halos may be observed (Figure 9b). The set of complete rings can be consistently indexed with the presence of an FCC-type phase (Fm3m). Only three rings of higher intensity are present, attributable to the presence of amorphous-associated halos that dim the intensity of the remaining rings. The other set of rings can be consistently indexed with the presence of Zr. As a remarkable

difference, rings in this set are not complete. This is perhaps due to mass differences between the Cu-Ni (which produces the Fm3m symmetrical crystallography phase) and Zr systems. Lower Zr mass produced lower reflections, so diffracted rings tend to be incomplete. The EDS of these particles revealed a stoichiometry of 66% Cu, 26% Ni, and 8% Zr (% at.). The amount of Cu measured by EDS is higher than the nominal value. Again, this may be due to the presence of Cu in the grid holding the sample or the inner parts of the TEM. The dark field shows crystallite size on the order of 6 nm. Average crystallite diameter was given through statistics as noted among different dark field micrographs of Cu-Ni-Zr particles. The average crystallite size is thus 5.9 ($\pm$ 3.3) nm over a total of 166 measures.
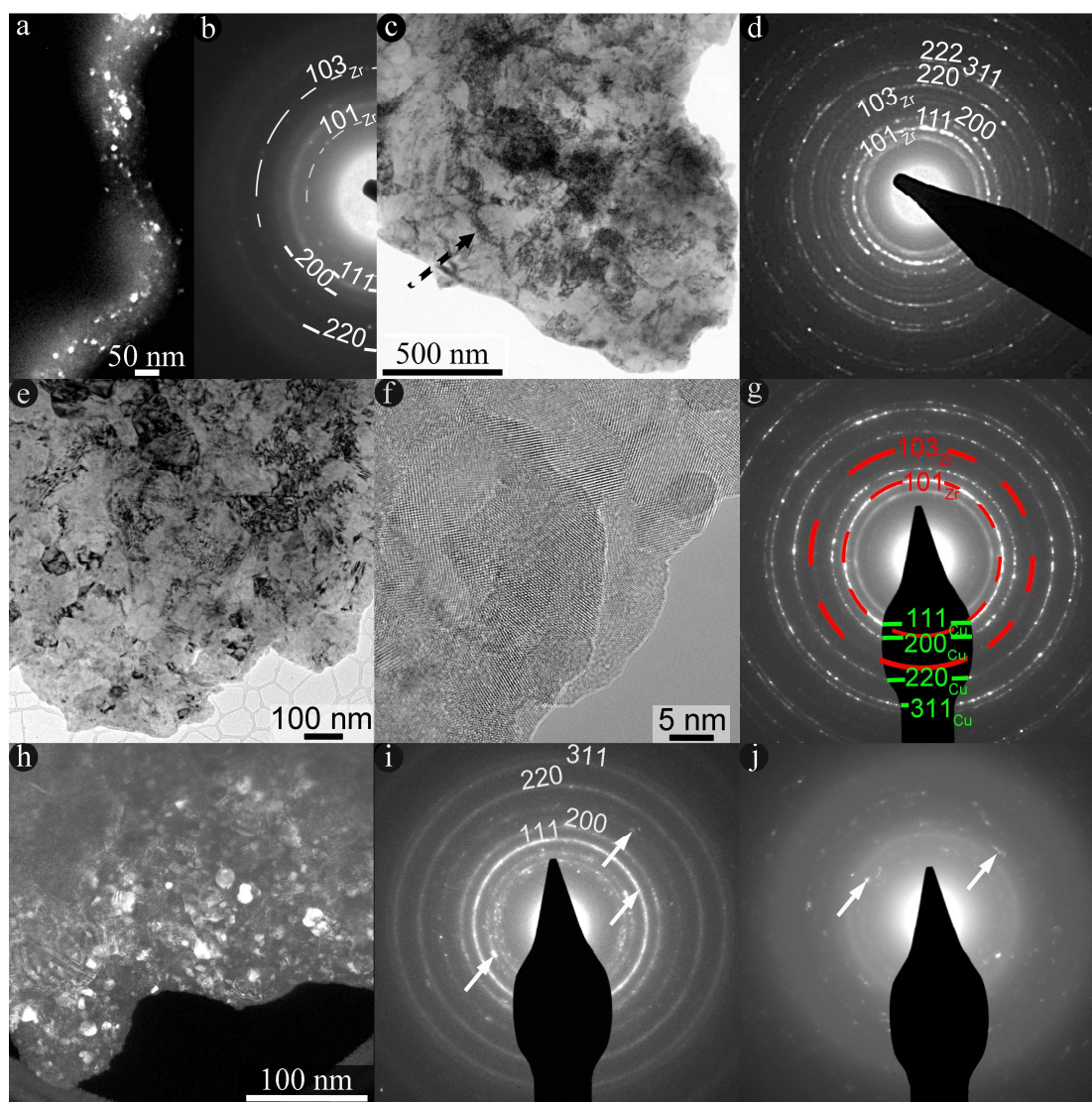
Figure 9. Images of bright field, dark field, and SAD of ternary alloy particles at 5 h milling time: Cu-33Ni-7Zr, a) dark field, b) left half SAD, c) bright field, and d) SAD; Cu-12Ni-23Zr, e) bright field, f) high resolution, g) SAD, h) dark field, i) SAD (crystalline zone), and j) SAD (amorphous zone)

The second type of particle (Figure 9c-d), though not as common, had SAD similar to that of Figure 9b. This SAD is formed by two sets of rings: one, which can be identified as belonging to the Fm3m spatial group; and another, belonging to spatial group P63/mmc,

similar to those of Zr. The morphology of this latter type of particle is also quite different– seemingly flat, i.e., at an average of 6 μm x 5 μm with a depth of only 300 nm. In addition, crystallite size is above 200 nm with many dislocations (dashed arrow, Figure 9c).

Again, X-Rays gave statistical information about the sample, which revealed an average crystallite size of 70 nm, and no crystalline Zr up to the range of detectability. However, since the TEM SAD were able give information about crystallites smaller than 5 nm, some Zr crystallites could be still detected in crystallite state (Figure 9d). The image in Figure 9b is in stark contrast with the amorphization suggested by the lack of Zr detected via XRD (Figure 2c). Moreover, the presence of some other particles with crystallite domains larger than 300 nm (Figure 9c) helps to explain the average crystallite size calculated using X-Ray diffractograms. The discrepancies between statistical XRD techniques and techniques with lower detectability ranges are common for intermediate milling stages [11].

In the case of Cu-12Ni-23Zr alloy at 5 h milling time, two types of particles were also present. The first type of particle was mainly composed of Cu, in which Zr oscillated between 1% at. and 23% at., and Ni was almost non-existent. Crystallite size for these particles was between 7 and 70 nm. They present zones with significant accumulation of dislocations close to crystallite boundaries (Figure 9e). The HRTEM image of this particle also showed the compact disposition of grains (Figure 9f).

The SAD for the first type of particles is shown in Figure 9g. The diffraction pattern has two sets of rings: one belonging to the FCC spatial group; the other, HCP, just like Zr. The second type of particle is equally abundant as the former. EDS shows Ni content variations between 11 at. % and 33 at. %. Generally, higher Ni content is in detriment to Zr content. The SAD of these particles suggest more or less amorphization as a function of Ni and Zr

present in each particle, as shown in Figures 9i and j. In other words, the SAD of particles

with more Zr are consistent with the presence of an amorphous phase. Moreover, the first

kind of particles, with no Zr, had crystallites under XRD detection limit or with high

dislocation increasing tension in the material. Increased tensions increase the $<\varepsilon>$ value in

X-Ray measurements. All these factors combined are compatible with the X-Ray

diffractogram of an amorphous material, as shown in Figure 2d.

3.4 Thermodynamic model

3.4.1. Solid solution

The Gibbs free energy of mixing (ΔG^m) of one system can be obtained by $\Delta G^m = \Delta H^m - T\Delta S^m$, where T is the temperature; and ΔH^m and ΔS^m are the enthalpy and entropy of

mixing. ΔH^m can be obtained as the sum of three terms, $\Delta H^m = \Delta H_c + \Delta H_{el} + \Delta H_{st}$, where

ΔH_c is the chemical contribution of formation and breaking of atomic bonds, ΔH_{el} is the

elastic contribution (elastic mismatch energy) in solid solutions, and ΔH_{st} is the

contribution of lattice stability energy due to differences in valence electrons of solute and

solvent atoms. The ΔH_c and ΔH_{el} contributions are much larger than the ΔH_{st} contribution,

and so ΔH_{st} was negligible. ΔS^m is configurational entropy, and can be calculated as

$\Delta S^m = -R\Sigma x_i \ln_i$, where R is the universal gas constant, and x_i is the mole fraction of element

i. Chemical contributions to mixing enthalpy in a multicomponent alloy can be estimated

by applying the semi-empirical model proposed by Miedema [41], which is widely used

due to its simplicity. In that model, ΔH_c for each binary system can be determined by

means of eq.(5), where V_A, V_B are the molar volumes of atoms A and B, respectively; ϕ^* is

the work function of the constituent elements; n_{ws} is the electron density; P, Q, and R' are

constants related to the constituent elements; and $f(C^S) = C_A{}^S C_B{}^S$, where $C_A{}^S$ and $C_B{}^S$ are

determined by eq. (6). Systematic deviation between the enthalpy of mixing obtained from

Miedema's model and experimental data in binary systems is expected, and so a pre-factor

$S(x)$ has been proposed to take significant atomic size difference effects into account, eq.

(7) [42]. There, C is an empirical parameter describing the effect of atomic size differences

semi-quantitatively; it is given as 0.5 and 2.0 for liquid alloys and ordered compounds,

respectively, and a value of 1 is given for disordered solid solutions.

$$\Delta Hc = 2 P f\left(C^S\right) S(x) \frac{\left(x_A V_A^{2/3} + x_B V_B^{2/3}\right)}{\left(n_{ws}^A\right)^{-1/3} + \left(n_{ws}^B\right)^{-1/3}} x \left[-\left(\Delta \phi^*\right)^2 + \frac{Q}{P}\left(\Delta n_{ws}^{1/3}\right)^2 - \frac{R'}{P}\right] \tag{5}$$

$$C_A^S = \frac{x_A V_A^{2/3}}{x_A V_A^{2/3} + x_B V_B^{2/3}} \qquad C_B^S = \frac{x_B V_B^{2/3}}{x_A V_A^{2/3} + x_B V_B^{2/3}} \tag{6}$$

$$S(x) = 1 - C \frac{x_A x_B \left|V_A - V_B\right|}{x_A^2 V_A + x_B^2 V_B} \tag{7}$$

ΔH_{el} can be calculated as in Bakker et al. [43], eq. (8), where $\Delta E_{A\,in\,B}$ is the elastic mismatch

energy caused by element A dissolved in element B, and $\Delta E_{B\,in\,A}$ is the elastic mismatch

energy caused by element B dissolved in element A. The $\Delta E_{i\,in\,j}$ values can be calculated

using eqs. (9), where K, G are the bulk and shear moduli, respectively.

$$\Delta He = x_A x_B \left(x_A \Delta E_{A\,in\,B} + x_B \Delta E_{B\,in\,A}\right) \tag{8}$$

$$\Delta E_{A\,in\,B} = \frac{2 K_A G_B \left(V_B - V_A\right)^2}{3 K_A V_B + 4 G_B V_A} \qquad \Delta E_{B\,in\,A} = \frac{2 K_B G_A \left(V_A - V_B\right)^2}{3 K_B V_A + 4 G_A V_B} \tag{9}$$

3.4.2. Amorphous phase

The Gibbs free energy of amorphization is given by $\Delta G^{am} = \Delta H^{am} + T \Delta S^m$, where ΔH^{am} is the

enthalpy of amorphization. The enthalpy of amorphization can be calculated by eq. (10),

where ΔHc is the chemical contribution and ΔH^{topo} is the topological enthalpy. In an

amorphous alloy, chemical and structural contributions to enthalpy of mixing are negligible

due to lack of crystal structure; rather, topological enthalpy takes the difference between

crystalline and amorphous states into account. Therefore, $\Delta H^{topo} = 3.5 \ (x_A T_A^m + x_B T_B^m)$ [44],

where T^m is the melting temperature of elements A and B.

$$\Delta H^{am} = \Delta Hc + \Delta H^{topo} \tag{10}$$

3.4.3. Extension to ternary systems

A general approach to obtain thermodynamic information in ternary systems is to

extrapolate from its constitutive binary systems. Extrapolation to ternary systems has been

used to reasonable success in previous papers [45,46]. In this work, Toop's model was

chosen due to its being an asymmetrical model and for its mathematical simplicity; it was

used to determine thermodynamic properties (Gibbs free energy and enthalpy) of the

ternary system (A-B-C) under study. This model is given in eq. (11), where Γ represents a

thermodynamic property, and ΔH^m_{A-B}, ΔH^m_{B-C}, ΔH^m_{C-A} are the thermodynamic properties of

mixing three binary systems. Parameters required to solve eqs. 5 to 11 for the Cu-Ni-Zr

system are listed in Table 2. In this work, crystallite size effects were not included; for

works including crystallite size effects on Gibbs free energy, see Bera et al. [46].

$$\Delta H^m = \left(\frac{x_B}{x_A + x_B} \right) \Delta H^m_{A\text{-}B} \left(x_A, 1 - x_A \right) + \left(\frac{x_C}{x_A + x_C} \right) \Delta H^m_{A\text{-}C} \left(x_A, 1 - x_A \right)$$
$$+ \left(x_B + x_C \right)^2 \Delta \Gamma^m_{B\text{-}C} \left(\frac{x_B}{x_B + x_C}, \frac{x_C}{x_B + x_C} \right) \tag{11}$$

Table 2. Parameters for thermodynamic analysis of Cu-Ni-Zr system [41]

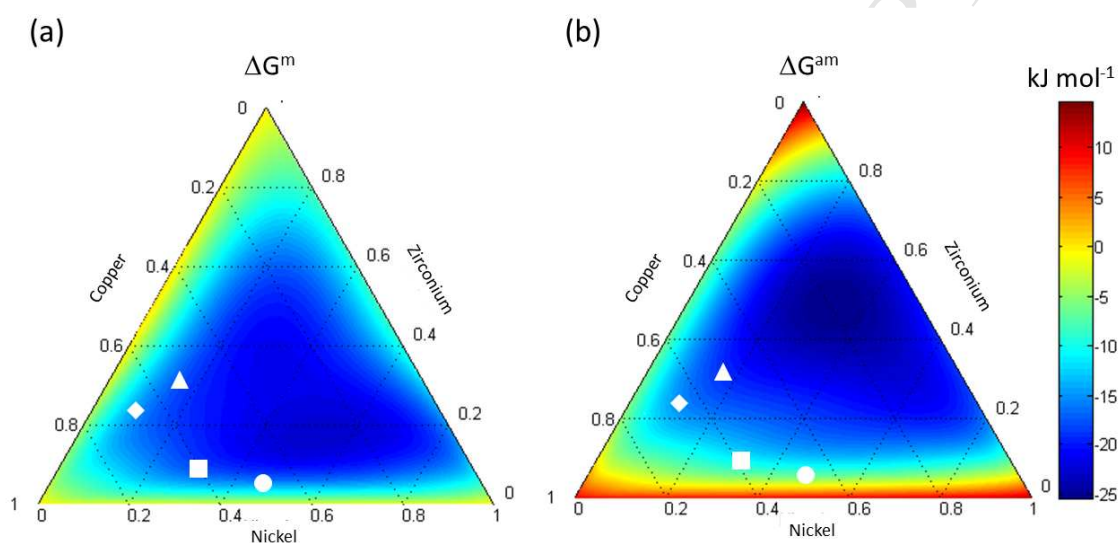|	$n_{ws}^{1/3}$ (cm^{-1})	Φ^* (V)	K (10^{10} Nm^{-2})	G (10^{10} Nm^{-2})	V (cm^3 mol^{-1})	T^m (K)	P (kJV^{-2} cm^{-1})	Q (kJV^{-1})	R'/P
Cu	1.47	4.45	13.7	4.83	7.1	1357	14.1	132.54	0
Ni	1.75	5.20	18.0	7.6	6.59	1728			
Zr	1.39	3.40	9.1	3.3	14.06	2128			

Figure 10. Gibbs free energy for (a) formation of solid solutions and (b) formation of amorphous phase of Cu-Ni-Zr systems. Compositions are in atomic percentages. ○: Cu-43Ni-7Zr, Δ: Cu-12Ni-31Zr, □: Cu-33Ni-7Zr, and ◊: Cu-12Ni-23Zr.

Figure 10a gives the calculated Gibbs free energy of mixing (ΔG^m) for the formation of solid solutions of the Cu-Ni-Zr system, whereas Figure 10b shows the Gibbs free energy (ΔG^{am}) for the formation of amorphous phase in the same ternary system. The main features of the Gibbs free energy of the formation of solid solution shown by Figure 10a include: i) higher Gibbs free energy values are in the corners (green/yellow zone), with values around 2 kJ mol^{-1}; ii) the triangle graph has a large area indicating negative ΔG^m

values (blue zone), i.e., there is a driven force to form solid solution from elemental

powders; and iii), the smallest ΔG^m is at approximately Cu-50Ni-18Zr (at.%). On other

hand, the features of the Gibbs free energy for the formation of amorphous phase are: i) the

highest Gibbs free energy values are similarly in the corners (red zone), with values

between 5 and 14 kJ mol^{-1}, in the Zr corner; ii) a large zone of negative ΔG^{am} values,

indicating amorphous phases can be formed from elemental powders, with a minimum of -

25 kJ mol-^{1} at approximately Cu-35Ni-50Zr (at.%); and iii) increases in Zr content

decreases ΔG^{am} values, suggesting amorphous phase formation increases as a function of

Zr, which is in agreement with XRD results.

The ΔG^m and ΔG^{am} values for the alloys with the highest nickel content are, for Cu-43Ni-

7Zr: ΔG^m= -12 kJ mol^{-1} and ΔG^{am} = -5 kJ mol^{-1}; and, for Cu-33Ni-7Zr: ΔG^m= -16 kJ mol^{-1}

and ΔG^{am} = -10 kJ mol^{-1}. These values indicate that there is a driving force for the

formation of a solid solution for alloys with higher nickel content. The ΔG^m and ΔG^{am}

values for greater Zr-containing alloys are, for Cu-12Ni-31Zr: ΔG^m= -16 kJ mol^{-1} and ΔG^{am}

= -20 kJ mol^{-1}; and, for Cu-12Ni-23Zr: ΔG^m= -12 kJ mol^{-1} and ΔG^{am} = -15 kJ mol^{-1}. These

values indicate that there is a driving force for the formation of an amorphous phase for

alloys with higher Zr content.

The thermodynamic data are in agreement with the XRD (Figure 2) and TEM (Figures 8

and 9) results. The XRD patterns showed that the amorphous phase is formed at shorter

milling times when Zr content increases. The MA of the Cu-Ni-Zr system can be explained

in three stages (I, II, and III), as shown in Figure 11. In stage I, the energy of system is

given by mixing of elemental powders. The peaks of elemental powders are clearly

observed in the XRD patterns and TEM images, showing larger and crystalline grains. In

stage II, powders are milled with increasing crystalline defect density. As milling time

increases, XRD patterns exhibit peak broadening, peak shift, and disappearance of peaks

(for solutes) due to severe plastic deformation [23]. At shorter milling times, the cold

welding process is more prominent than is the fracture process, so particle size increases; as

milling time increases, cold welding and fracture processes compete. At the end of stage II,

a solid solution of Cu, Ni, and Zr is formed due to decreases in Gibbs free energy. Finally,

in stage III, powder suffers severe plastic deformation as milling continues, due to the

collision of balls producing crystalline defects like dislocation, stacking faults, twins,

vacancies, and grain boundaries [47]. In this stage, the fracture process is predominant,

decreasing particle size. Strain energy increases as a function of milling time, until lattice

strain reaches a critical value and the formation of an amorphous phase is more favorable

than the formation of a solid solution (crystalline phase). The formation of an amorphous

phase is facilitated by high crystalline defect density promoting a faster diffusion process

through smaller atomic volume ratios [48]. The XRD patterns have a hump (Figure 2), and

the TEM diffraction patterns show diffuse rings, both indicating an amorphous phase.
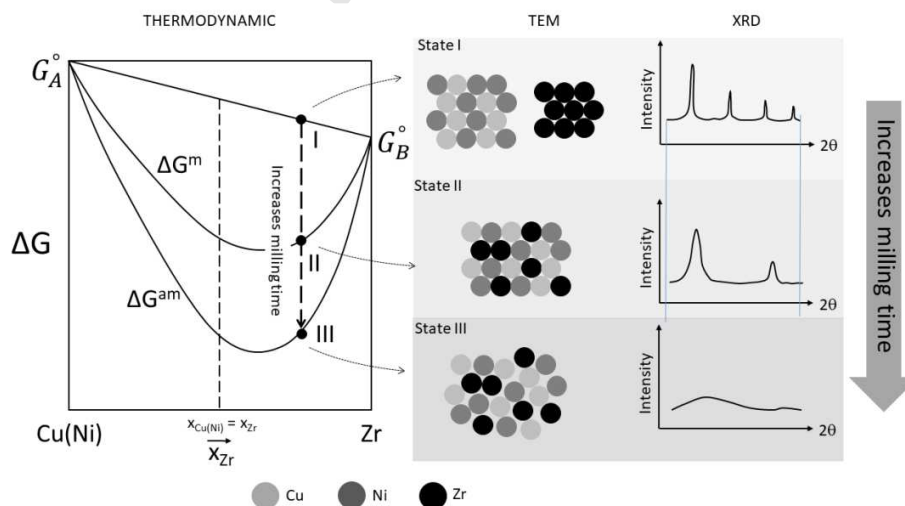
Figure 11. Schematic correlation between thermodynamic data and XRD and TEM results, explaining the formation of an amorphous phase.

CONCLUSIONS

The influence of quantities of nickel and zirconium on the amorphization of the Cu-Ni-Zr ternary alloy system was determined. In addition, the order of formation (Cu-Ni solid solution and the subsequent incorporation of Zr) was established. The crystallinity of this solution is influenced by the amount of Ni in the system, or rather, greater quantities of Zr results in less crystallinity; in brief, Zr promotes amorphous formation in the system.

The X-Ray patterns show a loss of crystallinity after 5 h of milling, though dependent on Zr content; nevertheless, TEM demonstrated that 5 hours of milling results rather in simultaneous and varied states of milling. Thus fabrication of Copper-based alloys prepared via mechanical alloying are not homogeneous, but occurs in stages.

Thermodynamic calculations with extended Miedema's models are in agreement with XRD and TEM results. Experimental and thermodynamic data showed that solid solutions are formed in a first stage, followed by the formation of an amorphous phase as milling time and Zr content increased.

With these results, milling conditions, and ternary alloys in mind, the most important variable in the production of amorphous structures is zirconium content.

Acknowledgements

REFERENCES

[1]   W. Klement, R.H. Willens, P. Duwez, Non-crystalline Structure in Solidified Gold–Silicon Alloys, Nature. 187 (1960) 869–870. doi:10.1038/187869b0.

[2]   A. Takeuchi, A. Inoue, Classification of Bulk Metallic Glasses by Atomic Size Difference, Heat of Mixing and Period of Constituent Elements and Its Application to Characterization of the Main Alloying Element, Mater. Trans. 46 (2005) 2817–2829. doi:10.2320/matertrans.46.2817.

[3]   C. Suryanarayana, Mechanical alloying and milling, Prog. Mater. Sci. 46 (2001) 1–184. doi:10.1016/S0079-6425(99)00010-9.

[4]   J. Eckert, J. Das, S. Pauly, C. Duhamel, Mechanical properties of bulk metallic glasses and composites, J. Mater. Res. 22 (2007) 285–301. doi:10.1557/jmr.2007.0050.

[5]   A. Inoue, W. Zhang, T. Zhang, K. Kurosaka, High-strength Cu-based bulk glassy alloys in Cu-Zr-Ti and Cu-Hf-Ti ternary systems, Acta Mater. 49 (2001) 2645–2652. doi:10.1016/S1359-6454(01)00181-1.

[6]   Y.C. Kim, J.C. Lee, P.R. Cha, J.P. Ahn, E. Fleury, Enhanced glass forming ability and mechanical properties of new Cu-based bulk metallic glasses, Mater. Sci. Eng. A. 437 (2006) 248–253. doi:10.1016/j.msea.2006.07.141.

[7]   J. Das, M.B. Tang, K.B. Kim, R. Theissmann, F. Baier, W.H. Wang, J. Eckert, "Work-Hardenable" Ductile Bulk Metallic Glass, Phys. Rev. Lett. 94 (2005) 1–4. doi:10.1103/PhysRevLett.94.205501.

[8]   H. min ZHAI, H. feng WANG, F. LIU, Effect of minor Nb addition on mechanical properties of in-situ Cu-based bulk metallic glass composite, Trans. Nonferrous Met. Soc. China (English Ed. 27 (2017) 363–368. doi:10.1016/S1003-6326(17)60040-2.

[9]   C. Suryanarayana, Nanocrystalline materials, Int. Mater. Rev. 40 (1995) 41–64.
doi:10.1179/imr.1995.40.2.41.

[10]   C. Suryanarayana, Mechanical Alloying and Milling, 2004.

[11]   C. Suryanarayana, A. Inoue, Bulk Metalic glasses, 2011.

[12]   X. Cui, F.Q. Zu, Z.Z. Wang, Z.Y. Huang, X.Y. Li, L.F. Wang, Study of the
reversible intermetallic phase: B2-type CuZr, Intermetallics. 36 (2013) 21–24.
doi:10.1016/j.intermet.2012.12.008.

[13]   C. Martínez, P. Rojas, C. Aguilar, D. Guzmán, E. Zelaya, Estudio de los cambios
microestructurales del Ni al ser sometido a molienda de alta energía, Rev. Mater. 20
(2015) 621–626. doi:10.1590/S1517-707620150003.0063.

[14]   P. Rojas, C. Martínez, F. Viancos, C. Aguilar, D. Guzmán, E. Zelaya, Fabricación de
vidrios metálicos base cobre: Evolución de las fases durante el proceso de aleación
mecánica, Rev. Mater. 20 (2015) 705–713. doi:10.1590/S1517-707620150003.0074.

[15]   P.A. Rojas, C. Martínez, C. Aguilar, F. Briones, M.E. Zelaya, D. Guzmán,
Characterization of phase changes during fabrication of copper alloys, crystalline
and non-crystalline, prepared by mechanical alloying, Ing. E Investig. 36 (2016)
102–109. doi:10.15446/ing.investig.v36n3.54224.

[16]   H.M. Rietveld, A profile refinement method for nuclear and magnetic structures, J.
Appl. Crystallogr. 2 (1969) 65–71. doi:10.1107/S0021889869006558.

[17]   J. Rodríguez-Carvajal, Recent advances in magnetic structure determination by
neutron powder diffraction, Phys. B Condens. Matter. 192 (1993) 55–69.
doi:10.1016/0921-4526(93)90108-I.

[18]   G.. Williamson, W.. Hall, X-ray line broadening from filed aluminium and wolfram,
Acta Metall. 1 (1953) 22–31. doi:10.1016/0001-6160(53)90006-6.

[19] T. Ungár, A. Borbély, The effect of dislocation contrast on x☐ray line broadening: A new approach to line profile analysis, Appl. Phys. Lett. 69 (1996) 3173–3175. doi:10.1063/1.117951.

[20] B.E. Warren, X-ray diffraction, Dover Publications Inc., 1990.

[21] B.D. Arias, J.P. Abrlata, Cu-Zr (Copper-Zirconium), Bull. Alloy Phase Diagrams. 11 (1990) 452–459.

[22] P. Nash, C. Jayanth, The Ni-Zr (Nickel-Zirconium) System, Bull. Alloy Phase Diagrams. 5 (1984) 144–148.

[23] T. Ungár, Microstructural parameters from X-ray diffraction peak broadening, Scr. Mater. 51 (2004) 777–781. doi:10.1016/j.scriptamat.2004.05.007.

[24] P.A. Rojas, A. Peñaloza, C.H. Worner, R. Fernandez, A. Zuñiga, Supersaturated Cu-Li solid solutions produced by mechanical alloying, J. Alloys Compd. 425 (2006) 334–338. doi:10.1016/j.jallcom.2006.01.032.

[25] J.A. Betancourt-Cantera, F. Sánchez-De Jesús, G. Torres-Villaseñor, A.M. Bolarín-Miró, C.A. Cortés-Escobedo, Extended solid solubility of a Co-Cr system by mechanical alloying, J. Alloys Compd. 529 (2012) 58–62. doi:10.1016/j.jallcom.2012.03.082.

[26] R. Hamzaoui, O. Elkedim, Magnetic properties of nanocrystalline Fe-10%Ni alloy obtained by planetary ball mills, J. Alloys Compd. 573 (2013) 157–162. doi:10.1016/j.jallcom.2013.03.183.

[27] A. Contini, F. Delogu, S. Garroni, G. Mulas, S. Enzo, Kinetics behaviour of metastable equiatomic Cu-Fe solid solution as function of the number of collisions induced by mechanical alloying, J. Alloys Compd. 615 (2015) S551–S554. doi:10.1016/j.jallcom.2013.11.232.

[28]   C. Aguilar, D. Guzmán, F. Castro, V. Martínez, F. De Las Cuevas, S. Lascano, T. Muthiah, Fabrication of nanocrystalline alloys Cu-Cr-Mo super satured solid solution by mechanical alloying, Mater. Chem. Phys. 146 (2014) 493–502. doi:10.1016/j.matchemphys.2014.03.060.

[29]   A. Kumar, K. Jayasankar, M. Debata, A. Mandal, Mechanical alloying and properties of immiscible Cu-20 wt.% Mo alloy, J. Alloys Compd. 647 (2015) 1040–1047. doi:10.1016/j.jallcom.2015.06.129.

[30]   Q. Fang, Z. Kang, An investigation on morphology and structure of Cu-Cr alloy powders prepared by mechanical milling and alloying, Powder Technol. 270 (2015) 104–111. doi:10.1016/j.powtec.2014.10.010.

[31]   P.A. Loginov, E.A. Levashov, V. V. Kurbatkina, A.A. Zaitsev, D.A. Sidorenko, Evolution of the microstructure of Cu-Fe-Co-Ni powder mixtures upon mechanical alloying, Powder Technol. 276 (2015) 166–174. doi:10.1016/j.powtec.2015.02.020.

[32]   I. Manna, P.P. Chattopadhyay, F. Banhart, H.J. Fecht, Solid state synthesis of amorphous and/or nanocrystalline Al40Zr40Si20alloy by mechanical alloying, Mater. Lett. 58 (2004) 403–407. doi:10.1016/S0167-577X(03)00511-1.

[33]   A. Samanta, I. Manna, P.P. Chattopadhyay, Phase evolution in Al-Ni-(Ti, Nb, Zr) powder blends by mechanical alloying, Mater. Sci. Eng. A. 464 (2007) 306–314. doi:10.1016/j.msea.2007.02.016.

[34]   I. Manna, P.P. Chattopadhyay, F. Banhart, H.J. Fecht, Development of amorphous and nanocrystalline Al65Cu35-xZrxalloys by mechanical alloying, Mater. Sci. Eng. A. 379 (2004) 360–365. doi:10.1016/j.msea.2004.03.010.

[35]   C.J. Hu, P.Y. Lee, Formation of Cu-Zr-Ni amorphous powders with significant supercooled liquid region by mechanical alloying technique, Mater. Chem. Phys. 74

(2002) 13–18. doi:10.1016/S0254-0584(01)00411-4.

[36]   J.C. de Lima, V.H. dos Santos, T.A. Grandi, P.C.T. D'Ajello, A. Dmitriev,
       Thermodynamic considerations about the formation of alloys by mechanical
       alloying, Phys. Rev. B - Condens. Matter Mater. Phys. 62 (2000) 8871–8877.
       doi:10.1103/PhysRevB.62.8871.

[37]   M.S. Khoshkhoo, S. Scudino, J. Bednarcik, A. Kauffmann, H. Bahmanpour, J.
       Freudenberger, R. Scattergood, M.J. Zehetbauer, C.C. Koch, J. Eckert, Mechanism
       of nanostructure formation in ball-milled Cu and Cu-3wt%Zn studied by X-ray
       diffraction line profile analysis, J. Alloys Compd. 588 (2014) 138–143.
       doi:10.1016/j.jallcom.2013.10.252.

[38]   J. Bhatt, B.S. Murty, On the conditions for the synthesis of bulk metallic glasses by
       mechanical alloying, J. Alloys Compd. 459 (2008) 135–141.
       doi:10.1016/j.jallcom.2007.04.242.

[39]   S. Brandstetter, P.M. Derlet, S. Van Petegem, H. Van Swygenhoven, Williamson-
       Hall anisotropy in nanocrystalline metals: X-ray diffraction experiments and
       atomistic simulations, Acta Mater. 56 (2008) 165–176.
       doi:10.1016/j.actamat.2007.09.007.

[40]   C. Aguilar, J. Marín, S. Ordóñez, D. Celentano, F. Castro, V. Martínez, Estudio
       estructural de polvos Cu-Cr aleados mecánicamente, Rev. Metal. 42 (2006) 334–344.

[41]   A.R. Miedema, Cohesion in alloys - Fundamental of a semi-empirical model, Phys.
       100B. (1980) 1–28. doi:http://dx.doi.org/10.1016/0378-4363(80)90054-6.

[42]   W.C. Wang, J.H. Li, H.F. Yan, B.X. Liu, A thermodynamic model proposed for
       calculating the standard formation enthalpies of ternary alloy systems, Scr. Mater. 56
       (2007) 975–978. doi:10.1016/j.scriptamat.2007.01.044.

[43] H. Bakker, G.F. Zhou, H. Yang, Mechanically driven disorder and phase transformations in alloys, Prog. Mater. Sci. 39 (1995) 159–241. doi:10.1016/0079-6425(95)00001-1.

[44] H. Bakker, Enthalpies in Alloys: Miedema's Semi-empirical Model, Trans Tech Publications, 1998.

[45] M. Rafiei, M.H. Enayati, F. Karimzadeh, Thermodynamic analysis of solid solution formation in the nanocrystalline Fe-Ti-Al ternary system during mechanical alloying, J. Chem. Thermodyn. 59 (2013) 243–249. doi:10.1016/j.jct.2012.12.008.

[46] S. Bera, S. Mazumdar, M. Ramgopal, S. Bhattacharyya, I. Manna, Prediction of enthalpy of formation and Gibbs energy change in pseudo-binary (Ti-Zr)(Fe-Cr)2 and pseudo-ternary (Ti-Zr)(Fe-Cr) 2-H system using extended Miedema model, J. Mater. Sci. 42 (2007) 3645–3650. doi:10.1007/s10853-006-1377-9.

[47] D. Guzmán, S. Ordoñez, D. Serafini, P.A. Rojas, C. Aguilar, M. Santander, Thermal stability of amorphous $Mg_{50}Ni_{50}$ alloy produced by mechanical alloying, J. Non. Cryst. Solids. 356 (2010). doi:10.1016/j.jnoncrysol.2009.10.002.

[48] N. Al-Aqeeli, C. Suryanarayana, M.A. Hussein, Formation of an amorphous phase and its crystallization in the immiscible Nb-Zr system by mechanical alloying, J. Appl. Phys. 114 (2013). doi:10.1063/1.4825325.

Highlights

- Study of phase evolution of elemental powders Cu, Ni and Zr by mechanical alloying
- Formation of Cu-Ni solid solution and then the incorporation of Zr was established
- The influence of Zr on the amorphization of Cu-Ni alloys has been established.
- Thermodynamic calculation confirms the results of XRD and TEM was performed.